Thwarting Marangoni instability in a viscoelastic liquid film via parametric forcing

I. B. Ignatius, B. Dinesh, G. F. Dietze, and R. Narayanan

Phys. Rev. Fluids **10**, 044001 — Published 17 April 2025

DOI: 10.1103/PhysRevFluids.10.044001

Thwarting Marangoni instability in a viscoelastic liquid film via parametric forcing

I. B. Ignatius[1], B. Dinesh[2], G. F. Dietze[3] and R. Narayanan[1]
[1] *Department of Chemical Engineering, University of Florida, Gainesville, FL 32611, USA*
[2] *Department of Chemical Engineering and Technology, Indian Institute of Technology-BHU, Varanasi, UP 221005, India*
[3] *Université Paris-Saclay, CNRS, FAST, 91405, Orsay, France.*

We explore how fluid elasticity affects the stabilization of an inherently unstable Marangoni-driven thin-film system through the application of parametric forcing. In the absence of elasticity, parametric forcing increases the threshold for the long-wave Marangoni instability mode in a thin liquid film, thereby stabilizing the system. A quiescent stable state is achievable within a finite forcing amplitude range, provided the forcing frequency is below a critical value. Outside this parameter range, the system is unstable on account of either Marangoni or Faraday instability. We find that the behavior for a film of viscoelastic liquid is different in two significant ways, as a result of fluid elasticity. Firstly, the neutral stability diagram in the amplitude versus frequency plane displays an island of stability, bounded by an upper and a lower frequency, as opposed to the Newtonian case, which displays only an upper frequency bound. Below the lower frequency bound and above the upper frequency bound, the film can be simultaneously subject to both Maranogni and Faraday instability. Secondly, fluid elasticity lowers the forcing amplitude at the neutral stability bound for both the Marangoni and Faraday instabilities, with a more significant reduction in the latter. As a result, both the threshold amplitude and the amplitude range for full stabilization of the thin-film system are reduced, which is attributed to the memory effect imparted by fluid elasticity.

I. *INTRODUCTION*

A liquid film that is heated from below beyond a critical temperature gradient, results in surface tension gradients upon perturbation. These gradients drive fluid motion along the interface, leading to deformations at the free surface. These deformations are more significant in thin films, eventually causing dry-out due to a long-wavelength surface-tension-driven or Marangoni instability [1]. Such instabilities are particularly undesirable during the deposition of optical films, a process that often relies on the use of viscoelastic fluids like polymeric solutions [2]. This study examines the physics involved in thwarting Marangoni instability in viscoelastic liquid films using parametric forcing and assuming the absence of phase change and gravitational effects.

In the case of Newtonian fluids under gravity it was shown by Vanhook et. al. (1997) [1], through linear stability calculations, that the threshold for long-wave instability increases with higher external gravitational acceleration. Based on this observation, past studies [3–5] have shown that external parametric forcing can also thwart this instability in Newtonian liquids. Most recently, Ignatius et. al. (2024) [3] revealed that a long-wavelength Marangoni instability can be quenched within a finite amplitude range if the system is oscillated below a certain cutoff frequency. Below this stabilization range, the fluid interface grows monotonically due to Marangoni instability, while beyond this region, the fluid exhibits significant undulations at the interface on account of resonance or Faraday instability [6]. In addition to these observations, it was noted that above the cutoff frequency, a quiescent stable state cannot be achieved as the fluid layer becomes unstable due to Faraday instability before complete stabilization is achievable.

In the current study, we extend the work of Ignatius et. al. [3] to viscoelastic fluids undergoing Marangoni instability. The main characteristic of such fluids is that their mechanical response is both elastic, allowing the storage of energy, and viscous, allowing the dissipation of energy. The memory effect associated with elasticity can be viewed as a form of inertia. This, in turn, can potentially cause the stabilization region to shift upon parametric forcing. Thus, the introduction of the elastic property distinguishes the current work from the previous studies in two significant ways. First, unlike the case of parametric forcing of Newtonian fluids, where forcing always has a stabilizing influence, we shall show that in viscoelastic fluids, parametric forcing can be either stabilizing or destabilizing. Second, our findings reveal the existence of an additional critical frequency that bounds the stabilization region between two frequency limits. We also show that the two necessary ingredients to predict this additional critical frequency are the finite width of the liquid container and the elastic characteristics of the fluid.

The manuscript is divided into two main sections. In section II, we discuss the mathematical model for the instability of a viscoelastic liquid in a configuration as described in Fig. 1. This is followed by a section where we examine the influence of parametric forcing on an unstable system of such a liquid due to Marangoni instability.

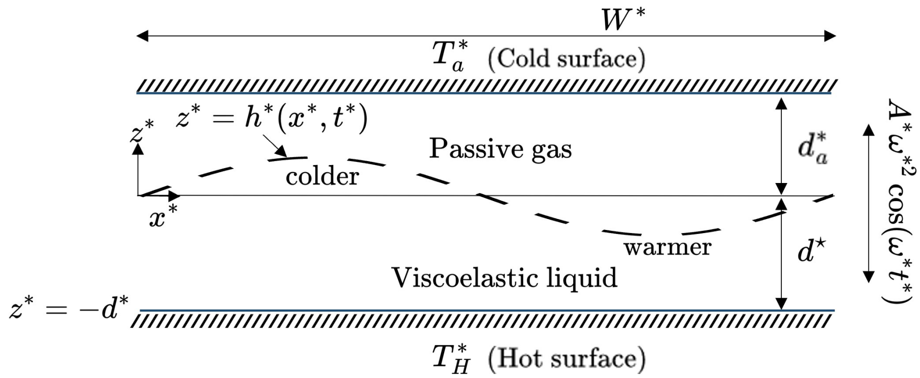

FIG. 1. Schematic of the studied configuration. A viscoelastic liquid layer that is heated from below and subject to a mechanical oscillation in the z-direction.

II. MATHEMATICAL MODEL

We consider a 2-dimensional viscoelastic liquid layer of unperturbed height, d^*, in a container of width, W^*, as shown in Fig. 1, where dimensioned variables are denoted by an asterisk hereafter. The liquid layer is in contact with a hydrodynamically passive ambient gas, denoted by the subscript 'a'. Gravity is assumed absent. The fluid system is heated from the liquid side by maintaining a constant temperature, T_H^*, and loses heat via the interface following Newton's law of cooling to an ambient gas confined by an upper wall kept at a temperature, T_a^*. Additionally, the fluid system is subjected to mechanical oscillations of angular frequency, ω^*, and amplitude, A^*, in the z-direction. The relevant thermophysical properties of the liquid are density, ρ, viscosity, μ, surface tension, γ, thermal conductivity, λ, and heat capacity, C_p. The liquid possesses a shear modulus, G, which imparts elastic character. The constitutive stress-strain relationship for the viscoelastic fluid is described by an upper-convected Maxwell equation [7]. This is expressed as

$$\boldsymbol{\tau}^* + \Lambda\left(\frac{\partial \boldsymbol{\tau}^*}{\partial t^*} + \mathbf{v}^* \cdot \boldsymbol{\nabla}^* \boldsymbol{\tau}^* - (\boldsymbol{\nabla}^* \mathbf{v}^*)^T \cdot \boldsymbol{\tau}^* - \boldsymbol{\tau}^* \cdot (\boldsymbol{\nabla}^* \mathbf{v}^*)\right) = \mu\Big(\boldsymbol{\nabla}^* \mathbf{v}^* + (\boldsymbol{\nabla}^* \mathbf{v}^*)^T\Big), \tag{1}$$

where $\Lambda = \frac{\mu}{G}$ is the relaxation time, and $\boldsymbol{\tau}^*$ and $\mathbf{v}^*$ represent the stress tensor and the velocity vector respectively.

Further, the surface tension of the liquid is assumed to decrease linearly with the free surface temperature according to

$$\gamma = \gamma_0 - \gamma_T (T^* - T_{i0}^*), \tag{2}$$

with $\gamma_T > 0$, the subscript 0 referring to the unperturbed base state and γ_0 denoting the surface tension at the corresponding unperturbed free surface temperature, T_{i0}^*.

We now proceed to give the scaled non-linear equations that govern this system, in a manner similar to [3].

A. Scaled non-linear equations

The variables x^*, z^*, and h^* are scaled with the characteristic length $l_c = d^*$. The variables, u^* and w^*, are made dimensionless with the velocity scale, $U_c = \gamma_0/\mu$, and the variables, t^* and ω^*, are scaled with a characteristic time, $t_c = d^*/U_c$. The pressure, p^*, and stress, $\boldsymbol{\tau}^*$, are scaled with the characteristic pressure, $p_c = \mu U_c/d^*$, and the temperature is scaled as $T = \frac{T^* - T_{i0}^*}{T_H^* - T_{i0}^*} = \frac{T^* - T_{i0}^*}{\Delta T^*}$. Note that $\Delta T^* = T_H^* - T_{i0}^*$ is treated as an input and may be obtained from the temperature difference between the bottom and top plates, as well as the heights and thermal conductivities of the fluid layers. Hereafter, the scaled variables are denoted without an asterisk.

Thus, the continuity and momentum equations are given by

$$\boldsymbol{\nabla}.\mathbf{v} = 0 \tag{3}$$

and

$$Re\Big(\frac{\partial \mathbf{v}}{\partial t} + \mathbf{v} \cdot \boldsymbol{\nabla} \mathbf{v}\Big) = -\boldsymbol{\nabla} p + \boldsymbol{\nabla} \cdot \boldsymbol{\tau} - \mathcal{A} cos(\omega t)\mathbf{e_z}, \tag{4}$$

where $\boldsymbol{\tau}$ is expressed by scaling the upper-convected Maxwell equation, i.e., Eq. (1), yielding

$$\boldsymbol{\tau} + De\left(\frac{\partial \boldsymbol{\tau}}{\partial t} + \mathbf{v}\cdot\boldsymbol{\nabla}\boldsymbol{\tau} - (\boldsymbol{\nabla}\mathbf{v})^T\cdot\boldsymbol{\tau} - \boldsymbol{\tau}\cdot(\boldsymbol{\nabla}\mathbf{v})\right) = \boldsymbol{\nabla}\mathbf{v} + (\boldsymbol{\nabla}\mathbf{v})^T. \tag{5}$$

In the above, three dimensionless groups appear, these are the Reynolds number, $Re = \frac{\rho U_c d^*}{\mu}$, the Deborah number, $De = \frac{\Lambda}{t_c} = \frac{\mu U_c}{G d^*}$, and a dimensionless parametric acceleration, $\mathcal{A}=\frac{\rho A^* \omega^{*2} d^{*2}}{\mu U_c}$. In addition to the domain equations, Eqs. (3) and (4), we have the energy equation given by

$$RePr\Big(\frac{\partial T}{\partial t} + \mathbf{v}\cdot\boldsymbol{\nabla}\mathbf{T}\Big) = \nabla^2 T, \tag{6}$$

where the Prandt number is given by $Pr = \frac{\mu C_p}{\lambda}$. The above equations are closed with appropriate boundary conditions.

At the bottom wall, $z = -1$, we impose no-slip and no-penetration conditions for velocity and hold the temperature fixed, i.e.,

$$\mathbf{v} = 0 \text{ and } T = 1. \tag{7}$$

At the impenetrable interface, $z = h(x,t)$, the jump mass balance and the jump momentum balance are given by

$$(\mathbf{v} - \mathbf{u})\cdot\mathbf{n} = 0 \tag{8}$$

and

$$-p\,\mathbf{n} + \mathbf{n}\cdot\boldsymbol{\tau} + \Big(\frac{1}{Ca} - MaT\Big)\,\mathbf{n}\boldsymbol{\nabla}\cdot\mathbf{n} + Ma\boldsymbol{\nabla_s}\mathbf{T} = 0, \tag{9}$$

where $\boldsymbol{\nabla_s}$ is the surface gradient operator, given by $\boldsymbol{\nabla} - \mathbf{n}(\mathbf{n}\cdot\boldsymbol{\nabla})$. The unit normal vector, $\mathbf{n}$, and the interface speed, $\mathbf{u}\cdot\mathbf{n}$, are given by

$$\mathbf{n} = \frac{-\dfrac{\partial h}{\partial x}\mathbf{e_x} + \mathbf{e_z}}{\left(1 + \left(\dfrac{\partial h}{\partial x}\right)^2\right)^{\frac{1}{2}}} \text{ and } \mathbf{u}\cdot\mathbf{n} = \frac{\dfrac{\partial h}{\partial t}}{\left(1 + \left(\dfrac{\partial h}{\partial x}\right)^2\right)^{\frac{1}{2}}}. \tag{10}$$

In addition to Eqs. 8 and 9, we assume Newton's law of cooling at the free surface via

$$\boldsymbol{\nabla T}\cdot\mathbf{n} + Bi(T - T_a) = 0. \tag{11}$$

which is similar to the interfacial heat transport condition adopted by Scriven and Sternling [8]. The above boundary conditions introduce three more dimensionless numbers. These are the capillary number, $Ca = \dfrac{\mu U_c}{\gamma_0}$, the Marangoni number, $Ma = \dfrac{\gamma_T \Delta T^*}{\mu U_c}$, and the Biot number, $Bi = \dfrac{\mathcal{H}\, d^*}{\lambda}$, where the heat transfer coefficient is defined from the conductive, quiescent state via $\mathcal{H} = \frac{\lambda_a}{d_a^*}$, with λ_a and d_a^* being the thermal conductivity and height of the gas layer and $T_a = \frac{T_a^* - T_{io}^*}{\Delta T^*}$. Observe that $Ca = 1$ for the chosen velocity scale and $\Delta T^* = (Bi/(Bi+1))(T_H^* - T_a^*)$. Next, we linearize the above scaled equations and then introduce spatial modal and Floquet expansions.

B. Linear stability analysis

The quiescent, conductive base state, denoted by subscripts 0, is given by

$$u_0 = w_0 = 0,\ \tau_{xx0} = \tau_{xz0} = \tau_{zz0} = 0,\ -\frac{\partial p_0}{\partial z} = \mathcal{A}cos(\omega t), -\frac{\partial T_0}{\partial z} = 1, \text{ and } h_0 = 0. \tag{12}$$

Assuming periodic conditions at the sidewalls, $x = 0$ and $x = W$, the unknown variables are linearized about the quiescent, conductive base state as

$$\psi = \psi_0 + e^{ikx} e^{\sigma t} \sum_{n=-N}^{n=N} \widehat{\psi}_n e^{(in\omega t)/2}, \tag{13}$$

where ψ corresponds to the dependent variables u, w, τ_{xx}, τ_{xz}, τ_{zz}, p, T and h, and where k and σ denote the disturbance wavenumbers and the inverse time constants respectively. The Floquet summations in time in Eq. (13) ensure compatibility with the harmonic forcing term in Eq. (4) [9].

Upon substitution of the forms given by (12) and (13) and dropping the summation terminology in Eqs. (14)-(20) and (22), the linearized equations become

$$ik\widehat{u} + \frac{\partial \widehat{w}}{\partial z} = 0, \tag{14}$$

$$Re\Big(\sigma + \frac{in\omega}{2}\Big)\widehat{u} = -ik\widehat{p} + ik\widehat{\tau}_{xx} + \frac{\partial \widehat{\tau}_{xz}}{\partial z}, \tag{15a}$$

$$Re\Big(\sigma + \frac{in\omega}{2}\Big)\widehat{w} = -\frac{\partial \widehat{p}}{\partial z} + ik\widehat{\tau}_{xz} + \frac{\partial \widehat{\tau}_{zz}}{\partial z}, \tag{15b}$$

$$RePr\Big[\Big(\sigma + \frac{in\omega}{2}\Big)\widehat{T} - \widehat{w}\Big] = -k^2\widehat{T} + \frac{\partial^2 \widehat{T}}{\partial z^2}, \tag{16}$$

$$\widehat{\tau}_{xx} + De\Big(\sigma + \frac{in\omega}{2}\Big)\widehat{\tau}_{xx} = 2ik\widehat{u}, \tag{17a}$$

$$\widehat{\tau}_{xz} + De\Big(\sigma + \frac{in\omega}{2}\Big)\widehat{\tau}_{xz} = \frac{\partial \widehat{u}}{\partial z} + ik\widehat{w}, \tag{17b}$$

and

$$\widehat{\tau}_{zz} + De\Big(\sigma + \frac{in\omega}{2}\Big)\widehat{\tau}_{zz} = 2\frac{\partial \widehat{w}}{\partial z}. \tag{17c}$$

At the bottom wall, $z = -1$, we have

$$\widehat{u} = 0, \;\; \widehat{w} = 0 \;\text{ and }\; \widehat{T} = 0. \tag{18}$$

The linearized boundary conditions at the interface, $z = 0$, are

$$\widehat{w} = \Big(\sigma + \frac{in\omega}{2}\Big)\widehat{h}, \tag{19}$$

$$\widehat{\tau}_{xz} = -ikMa\Big(\widehat{T} - \widehat{h}\Big), \tag{20}$$

$$\sum_{n=-N}^{n=N} e^{\frac{in\omega}{2}t} \Big\{ -\hat{p}_n + \mathcal{A}\cos(\omega t)\hat{h}_n + \widehat{\tau}_{zzn} = -k^2 \frac{1}{Ca}\hat{h}_n \Big\} = 0, \tag{21}$$

and

$$\frac{\partial \widehat{T}}{\partial z} + Bi(\,\widehat{T} - \widehat{h}) = 0. \tag{22}$$

TABLE I. Physical parameters used in the calculations. Fluid properties correspond to 0.5% wt./vol. aqueous polyacrylamide solution [10, 11], resulting in $De/Re = 2$, a dimensionless number independent of timescale.

Physical property	Symbol	Value
Viscosity	μ	$0.28\,\mathrm{Pa\,s}$
Shear modulus	G	$1.55\,\mathrm{Pa}$
Density	ρ	$1000\,\mathrm{kg\,m^{-3}}$
Surface tension	γ_0	$0.074\,\mathrm{N\,m^{-1}}$
Thermal conductivity	λ	$0.6\,\mathrm{W\,m^{-1}\,K^{-1}}$
Specific Heat	Cp	$4184\,\mathrm{J\,kg^{-1}\,K^{-1}}$
Film thickness	d^*	$5\times10^{-3}\,\mathrm{m}$
Air thickness	d_a^*	$1\times10^{-3}\,\mathrm{m}$

TABLE II. Typical values of dimensionless groups used in the calculation.

Dimensionless groups	**Value**
Re	5
De	10
Ca	1
Pr	2000
Bi	0.2

Observe that the summation symbol has been reintroduced in the Eq. 21 on account of the presence of $\mathcal{A}\cos(\omega t)$ term. The unknown dependent variables $\widehat{u}$, $\widehat{w}$, $\widehat{\tau}_{xx}$, $\widehat{\tau}_{xz}$, $\widehat{\tau}_{zz}$, $\widehat{p}$ and $\widehat{T}$ are discretized along the z-direction by expressing them in terms of Lagrange polynomials of order N_z and subsequently evaluating the domain equations at the corresponding Chebyshev Gauss-Lobatto collocation points [12]. This is done for all $n \in [-N, N]$, yielding a generalized eigenvalue problem of the form

$$\mathbf{A}\mathbf{x} = \sigma \mathbf{B}\mathbf{x}, \tag{23}$$

with eigenvalues $\sigma = \sigma_r + i\sigma_i$ and eigenvectors, $\mathbf{x}$. Here, σ_r is the temporal growth rate and σ_i the corresponding linear frequency shift with respect to the forcing frequency, ω. The eigensystem (23) is solved numerically for σ at given values of ω, k, $\mathcal{A}$ and Ma, using the `Eigenvalues` routine in Mathematica®. The neutral stability bounds, i.e., $\sigma_r = 0$, are obtained by finding a set of input parameters, say, $\mathcal{A}$ or Ma, for assigned values of ω and k. For example, to determine the critical Marangoni number, Ma_c, we fix the values of ω, k, and $\mathcal{A}$ and increment the Marangoni number until it reaches a critical value, where σ_r becomes zero. Likewise, the critical forcing amplitude, $\mathcal{A}_c$, is determined by incrementing the forcing amplitude until σ_r becomes zero for fixed values of ω, k and Ma. It was observed by numerical calculations that at these critical values, one of the eigenvalues, $(\sigma_r, \sigma_i) = (0, 0)$, implying exchange of stability at the neutral point. The coefficients of the Floquet summation corresponding to the interface deflection, $\{\widehat{h}_N, \widehat{h}_{N-1} .., \widehat{h}_{-N}\}$ obtained from the eigenvector, $\mathbf{x}$, tells us the interfacial temporal response upon instability. If the coefficient, $\widehat{h}_n$, corresponding to $n = 0$ is dominant compared to other coefficients, then the response is said to be "monotonic". However, if the coefficient, $\widehat{h}_n$, corresponding to $n \neq 0$ is dominant compared to $\widehat{h}_0$, then the response is "oscillatory". In particular, if the coefficients of the even index are zero then the response is subharmonic and if the coefficients of odd index are zero then the response is harmonic. For the calculations performed in the current study, it was found that the oscillatory response was subharmonic, with the dominant coefficient being $\widehat{h}_1$.

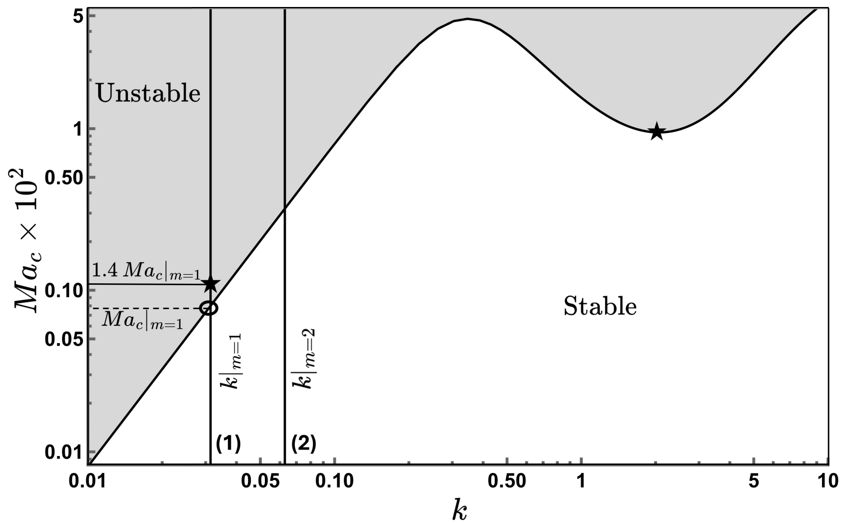

FIG. 2. Critical Ma vs. k curves in the absence of parametric forcing for an aqueous solution of polyacrylamide (PAAM), whose properties are given in Table I. The allowable wavenumbers $k = 2m\pi/W$ where $W = 200$ are denoted by vertical lines. The first two modes $m = 1$ and $m = 2$ are depicted.

III. RESULTS AND DISCUSSION

In the current section, we present the results of our linear stability calculations. Unless otherwise mentioned, these calculations were performed for a particular viscoelastic fluid, i.e. an aqueous solution of polyacrylamide (PAAM). The thermophysical properties of this fluid are given in Table I and the corresponding values for the dimensionless groups are given in Table II. In the first subsection, we will revisit the classical result for the neutral stability bound of the Marangoni instability in the absence of parametric forcing, noting that this bound is unaltered by elasticity [13–16]. This will set the stage for the second subsection, where we shall discuss the effect of elasticity on the neutral stability bound of Marangoni instability in the presence of parametric forcing, now noting that the Faraday instability threshold on isothermal fluids is affected by fluid's elasticity [17–20].

Linear stability in the absence of forcing

Unlike resonant instability, where the neutral stability bound is significantly influenced by the inertia associated with the momentum of the fluid (scaled by the Reynolds number, Re), the threshold for Marangoni instability, arising from a quiescent base state, is independent of the Reynolds number. This can be seen from Eqs. (15a) and (15b), which are independent of Re when σ, ω and $\mathcal{A}$ are set to zero. Likewise, examining Eqs. (17a) - (17c) reveals that the threshold for Marangoni instability, in the absence of forcing (ω=0), is independent of elasticity (scaled by the Deborah number, De).

Figure 2, plotted on a log scale, represents this threshold in the form of a critical curve, relating the Marangoni number to the wave number, which separates the regions of stability and instability. The initial rise and fall of this curve results from the competition between the destabilizing effect of surface tension gradients (via the tangential component of the force balance in Eq. 9) and the stabilizing effect of surface tension (via the interface curvature in the normal component of the force balance in Eq. 9). In the rising region, surface tension preferentially selects long waves upon instability. Beyond this wave number range, instability gives rise to short cellular patterns, and, for sufficiently large wave numbers, the critical curve rises once again due to the stabilization afforded by viscous and thermal diffusion [8].

The wavelength of the patterns observed upon instability also depends on the container width, W, as well as the sidewall conditions, which select the permissible waveforms. For a fixed container width, assuming periodic conditions at the side walls, the permissible waveforms are confined to one-full wave, two-full waves, three full waves, etc., i.e. $k = 2m\pi/W$, where $m \in \mathbb{N}$. In Fig. 2, where we have set $W = 200$, the permissible waveforms are marked by the vertical lines. Notice that among all permissible waveforms, the one-full wave form has the lowest critical Marangoni number (denoted by an open circle), even lower than the short-wave minimum (denoted by a star). Thus, if the Marangoni number is set to $Ma = 1.4Ma_c|_{m=1}$, denoted by the point where the vertical and horizontal solid lines

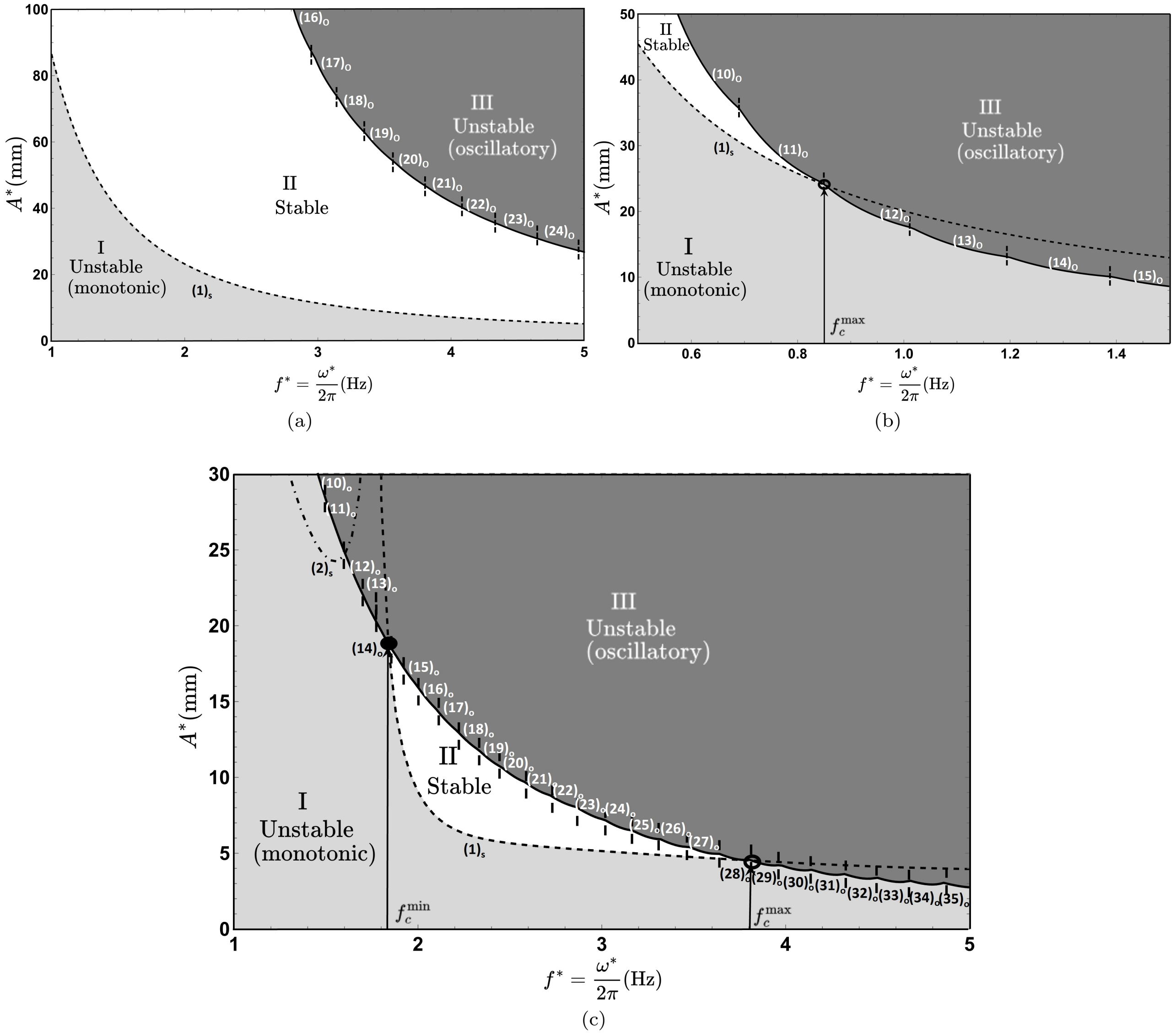

FIG. 3. Stability diagrams in the forcing amplitude versus forcing frequency plane: $W = 200$, $Ma = 1.4Ma_c|_{k=2\pi/W}$. (a) Newtonian fluid ($De = 0, Re = 5$) with properties according to Table I, (b) Newtonian fluid ($De = 0, Re = 50$), (c) viscoelastic polymeric solution according to Table I with $De = 10$ and $Re = 5$. Integers, m, in between parentheses identify the most unstable wave number $k{=}2m\pi/W$. Dashed curves: threshold for stabilization of the $m{=}1$ (monotonic) Marangoni instability mode via parametric forcing; solid curves: neutral instability bound for the (oscillatory) Faraday instability; dot-dashed curve: neutral instability bound for the $m{=}2$ (monotonic) Marangoni instability mode.

intersect in Fig. 2, the system becomes unstable exhibiting one-full wave pattern at the free surface. It might be noted that the small values of the critical Marangoni number that are depicted in Fig. 2 are due to the choice of velocity scale, set so that $Ca = 1$. It might be noted that the typical temperature drop across a bi-layer of the fluid under consideration and air required for the onset of instability at a Biot number of 0.2 is roughly 2 °C and therefore within an experimentally achievable range.

Linear stability in the presence of forcing

We now turn to the configuration where the heated liquid film is subject to parametric forcing. In this case, there are two instabilities to consider: the Marangoni instability, characterized by a monotonic growth of the interface over time, and the Faraday instability, which is typically oscillatory in nature. In Ignatius et. al. [3], we showed for a Newtonian fluid that parametric forcing, if tuned correctly, can suppress the Marangoni instability, without triggering the Faraday instability, thus leading to a fully quiescent state. In the current section, we show that this behaviour is greatly modified by fluid elasticity. To demonstrate this, we set the dimensionless container width, W, to $W = 200$ and the Marangoni number, Ma, to $Ma = 1.4Ma_c|_{k=2\pi/W}$. Thus, according to Fig. 2, only the waveform corresponding to $m = 1$ is unstable in the absence of forcing. Next, we apply parametric forcing and determine how this affects the stability diagram.

Figures 3a and 3b represent stability diagrams in the forcing amplitude, A^*, versus forcing frequency, f^*, for the limiting case of a Newtonian fluid (where De=0) at two values of the Reynolds number, Re. This allows us to see the effect of inertia in the Newtonian fluid case, before we advance to the viscoelastic case where elasticity also plays a role in the fluid's inertia. The dashed curves in Figs. 3a and 3b, correspond to the critical amplitude, A^*_s, for suppressing the Marangoni instability [3], whereas the solid curves represent the critical amplitude of the Faraday instability, A^*_o. The latter is a concatenation of line segments associated with the neutral bound of the least stable spatial mode, $k = 2m\pi/W$, at a given frequency, f^*, which is identified by the wave number index, m, placed between parentheses. These two curves demarcate three regions, denoted by Roman numerals, exhibiting different linear responses: (I) monotonic growth due to Marangoni instability; (II) full stability; (III) oscillatory growth due to Faraday instability. Comparing Figs. 3a (Re=5) and 3b (Re=50), we see that region (II) is reduced upon increasing Re, as a result of the dashed and solid curves intersecting. We designate the frequency at the intersection as *upper critical frequency* [3], $f_c^{\max}$. We now turn to Fig. 3c, which shows how this stability behaviour is affected by fluid elasticity. Here, all parameters are the same as in Fig. 3a, except for the Deborah number, De, which is set to De=10, according to the fluid properties in table I. Comparing Figs. 3a and 3c, we observe two main differences between the Newtonian and viscoelastic cases. Firstly, there is a second intersection between the dashed and solid curves in Fig. 3c, and we designate the corresponding frequency as the *lower critical frequency*, $f_c^{\min}$. As a result, region (II) has evolved into an island of stability, bounded by the lower and upper critical frequencies. Secondly, at sufficiently low frequencies, suppression of the Marangoni instability via parametric forcing becomes impossible (the dashed curve diverges). Instead, upon increasing the forcing amplitude in this frequency range, more and more monotonic spatial modes become unstable. We have represented the neutral stability bound for one of these modes, m=2, with a dot-dashed curve in Fig. 3c.

To understand the various features of the neutral stability diagram in Fig. 3c, let us first consider the region where the forcing frequency lies beyond the upper critical frequency. The fluid system remains unstable here to a waveform, $m = 1$, with a monotonic response to each forcing amplitude until the dashed curve is reached. However, a solid curve is seen below the dashed curve in this region. Here, shorter waveforms (m>28) with an oscillatory response become unstable due to Faraday instability. Thus, for frequencies greater than the upper critical frequency, the system exhibits a monotonic response for amplitudes below the solid curve and an oscillatory response for amplitudes above the solid curve. Next, we consider a frequency in between the two critical frequencies. Upon increasing the forcing amplitude in this range, the fluid system evolves from being monotonically unstable to an $m = 1$ waveform (below the dashed curve), via a stable quiescent conductive state (between dashed and solid curves), to short oscillatory waves due to Faraday resonance (beyond the solid curve). Finally, we examine the case of a low forcing frequency, i.e. a frequency below the lower critical frequency. In this frequency range, instead of stabilizing the $m = 1$ waveform, parametric forcing destabilizes a shorter $m = 2$ waveform, which also exhibits a monotonic response (above the dot-dashed curve). A further increase in forcing amplitude, beyond the solid curve will once again result in an oscillatory response due to Faraday instability.

Observe that the stabilization parameter range (region II) is smaller for a viscoelastic fluid (Fig. 3c) than for a Newtonian fluid (Fig. 3a). This is principally due to two reasons. First, the inertial action provided by the fluid's memory, as characterized by its elasticity, lowers both A^*_s and A^*_o, but lowers A^*_o at a faster rate. In essence, the fluid's elasticity reduces the threshold for stabilization, but also the parameter range in which stabilization is possible. Second, as just noted in Fig. 3c, for viscoelastic fluids, the dashed and solid curves intersect at *two* critical frequencies, causing the stabilization region to disappear when the parametric frequency is either decreased below the lower critical frequency (denoted by $\bullet$) or increased above the upper critical frequency (denoted by $\circ$). By contrast, for Newtonian fluids, the stabilization region increases with a decrease in parametric frequency and is only bounded by a single cutoff [3]. This cutoff frequency is not visible in Fig. 3a because the absence of elasticity-induced inertia within the high-viscosity Newtonian fluid (low Re) results in significantly large A^*_o and therefore a very large cutoff frequency ($f^* >> 100$Hz). This cutoff, which corresponds to the upper critical frequency, similarly observed in the case of viscoelastic fluids is depicted by $\circ$ in Fig. 3b, drawn for a higher Reynolds number.

The occurrence of two critical frequencies in viscoelastic fluids is viewed next from another perspective using the neutral curves, A^* vs k and Ma vs k. To this end, we turn first to the discussion of the upper critical frequency, $f_c^{\max}$, as the occurrence of this critical frequency is common to both Newtonian and viscoelastic fluids.

The origin of the upper critical frequency, $f_c^{\max}$, is illustrated using the A^* vs k graphs in Fig. 4, plotted for two frequencies on either side of this critical frequency, say $f^* = 3.5$Hz and $f^* = 4$Hz. In this figure, the dashed curves

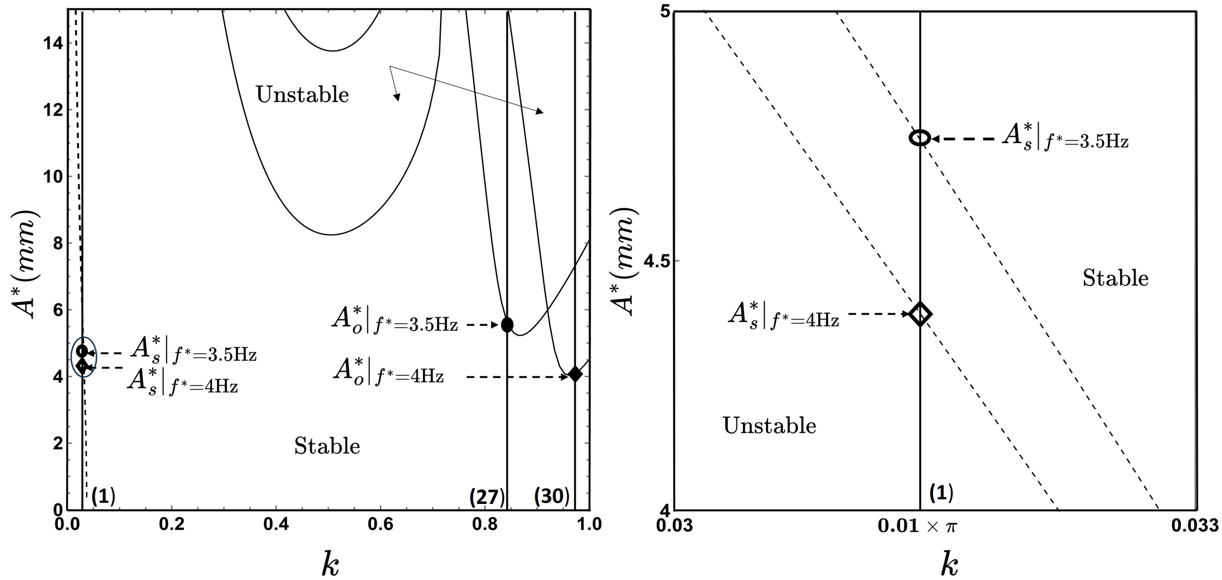

FIG. 4. Graphs illustrating the existence of the upper critical frequency, $f_c^{\max}(f^* = 3.8\text{Hz})$, depicted by $\circ$ in figure 3. Critical A^* versus k curves for two frequencies from Fig. 3c: Ma=$1.4Ma_c|_{m=1}$, $W = 200$, circles ($\circ$): f^*=3.5 Hz, diamonds $\Diamond$: f^*=4 Hz. Vertical lines mark the most unstable allowable waveforms, identified by m=$kW/2\pi$ (shown between parentheses). The figure on the right is a magnified view of the long-wave range in the left figure.

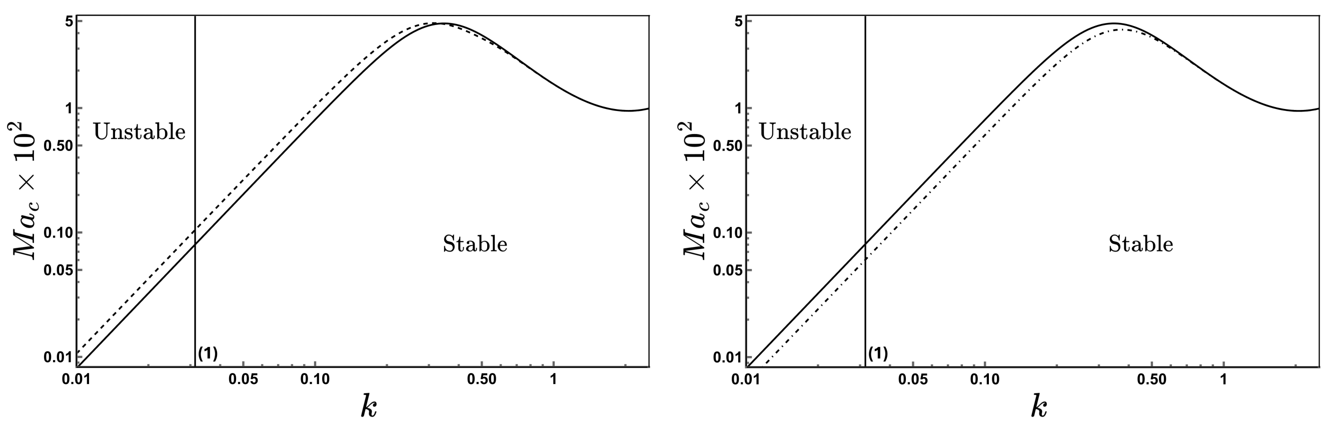

(a)

(b)

FIG. 5. Graphs illustrating the existence of the lower critical frequency, $f_c^{\min}$ ($f^* = 1.8\text{Hz}$), depicted by $\bullet$ in figure 3. Critical Ma vs k curves are plotted for frequencies, $f^* = 2\text{Hz}$ in panel (a) and $f^* = 1\text{Hz}$ in panel (b) to illustrate the stabilizing effect with an increase in forcing amplitude for frequencies greater than the $f_c^{\min}$ and a destabilizing effect for frequencies higher than $f_c^{\min}$. The vertical line represents the first permissible waveform. Here the amplitude of shaking is increased from $\mathcal{A} = 0$ (solid curve) to $\mathcal{A} = 0.5\mathcal{A}_c$ (dashed curve for $f^* = 2\,\text{Hz}$ and dot-dashed curve for $f^* = 1\,\text{Hz}$). $\mathcal{A}_c$ is the lowest critical amplitude among all the permissible waveforms, k=$2m\pi/W$, obtained in the absence of any heating.

represent the threshold required for stabilization of the monotonic mode, A^*_s, due to Marangoni instability and the tongue-like curves represent the critical amplitude, A^*_o, for the onset of an oscillatory instability due to resonance. Notice that A^*_o is higher than A^*_s at $f^* = 3.5\text{Hz}$ but lower at $f^* = 4\text{Hz}$. Thus there must exist a critical frequency for which $A^*_o = A^*_s$. Beyond this frequency, an oscillatory instability due to resonance occurs before complete stabilization is possible. The rapid decrease in A^*_o with frequency compared to A^*_s is attributed to increased momentum-induced inertia that promotes resonant oscillations at the fluid interface. Examining Fig. 4 reveals two necessary ingredients for predicting this critical frequency: These are the presence of the permissible wavenumbers on account of finite container width and the existence of the resonant "tongues".

Turning to the origin of the lower critical frequency, $f_c^{\min}$, denoted by $\bullet$ at $f^* = 1.8\text{Hz}$ in Fig. 3c, we consider

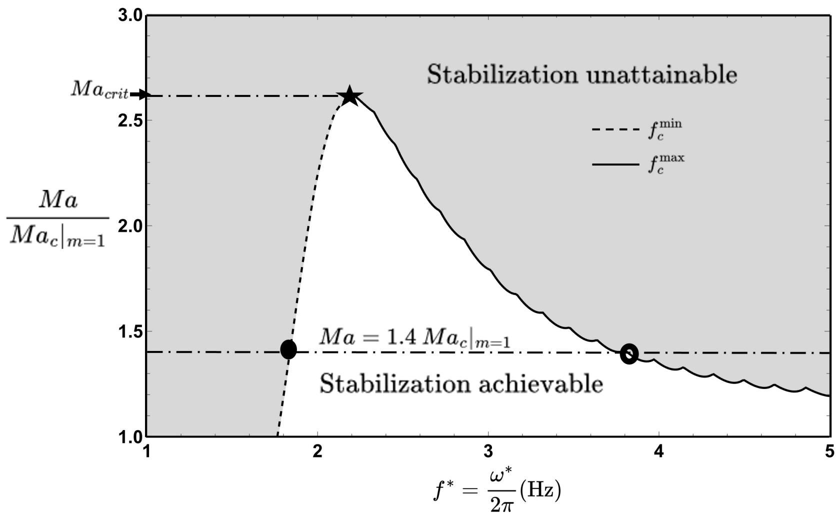

FIG. 6. Ma/Ma_c vs f_c depicting the Marangoni number and forcing frequency parameter space for which the stabilization is achievable. The trends of $f_c^{\min}$ and $f_c^{\max}$ are depicted using dashed and solid curves respectively. The $\star$ denotes the Marangoni number at which $f_c^{\max} = f_c^{\min}$.

the Ma vs k graphs plotted on a log-scale in Fig. 5. These graphs are plotted for two frequencies on either side of this critical frequency, viz., $f^* = 2$Hz (Fig. 5a) and $f^* = 1$Hz (Fig. 5b). At $f^* = 2$Hz, the threshold for long-wave Marangoni instability increases with increasing forcing amplitude, indicating the stabilization of the system. In contrast, at $f^* = 1$Hz, an increase in forcing amplitude further destabilizes the system, lowering the threshold for long-wave Marangoni instability. As a result, at frequencies below $f_c^{\min}$, a system that is inherently Marangoni-unstable cannot be stabilized, establishing a lower bound for the island of stability drawn in figure 3c. The reduction of the Marangoni threshold at frequencies below $f_c^{\min}$ causes shorter waveforms to become unstable as illustrated via the dot-dashed curve in Fig. 3c, where the onset of 2-full waves with a monotonic temporal response is observed.

The destabilizing effect induced by parametric forcing at lower frequencies is attributed to the counteracting elastic and viscous effects against the momentum-induced inertia. Although not plotted here, the $f_c^{\min}$ decreases with a decrease in elasticity or the Deborah number and disappears below a critical value, De_c. Thus, for weakly elastic fluids with $De < De_c$, and Newtonian fluids (where $De = 0$), parametric forcing always raises the threshold for long-wave instability; consequently, only one critical frequency, (corresponding to the upper critical frequency) appears. On the other hand, for viscoelastic fluids with $De > De_c$, the stabilization region is bounded between two critical frequencies.

The stabilization region however will disappear at large enough Marangoni numbers since an increase in temperature gradient requires a higher stabilization threshold, A_s^*. Therefore, the dashed curve in Fig. 3c shifts upwards, while the solid curve only changes slightly with the Marangoni number. Consequently, $f_c^{\max}$ shifts towards the left for a higher input Marangoni number, while $f_c^{\min}$ shifts only slightly to the right. This result is illustrated in Fig. 6 by plotting the Marangoni number as a function of critical frequencies, with the dashed curve representing $f_c^{\min}$ and the solid curve representing $f_c^{\max}$. The choppiness observed in the solid curve is related to the concatenation of the A_o^* vs f^* curve in Fig. 3c. At a distinct Marangoni number in our example ($Ma_{crit} \approx 2.6 Ma_c|_{m=1}$), the two curves coincide, i.e., $f_c^{\max}$ equals $f_c^{\min}$, causing the island of stability to vanish entirely. Clearly, for Ma beyond Ma_{crit} depicted using a $\star$ in Fig. 6, stabilization is impossible for all forcing frequencies. By contrast, in Newtonian fluids, $f_c^{\min}$ is absent and the stabilization region never completely disappears with an increase in Marangoni number (cf. Fig. 8 in Ignatius et. al. [3]).

IV. SUMMARY

The influence of a fluid's elasticity on stabilizing Marangoni-driven instabilities of viscoelastic layers through parametric forcing has been studied. Our findings are contrasted with the case of Newtonian fluids where it is known that parametric forcing raises the threshold for long-wave Marangoni instability, thereby stabilizing it [3–5]. Past investigations by Ignatius et. al.(2024) [3] for such fluids have revealed that complete stabilization and the subsequent suppression of dry-out can be achieved within a finite range of amplitude. This amplitude range increases as frequency decreases. Below this amplitude range, the fluid interface grows monotonically on account of Marangoni instability, while above this range, the fluid interface exhibits resonant oscillations due to Faraday instability. However, beyond a certain critical frequency, the stabilization region completely vanishes since the Faraday instability threshold becomes lower than that required to suppress Marangoni instability. In contrast, for viscoelastic fluids, the transient dynamics and the emergence of a stabilization region are altered in two significant ways.

First, unlike in Newtonian fluids where the stabilization region is bounded by a single critical frequency, in viscoelastic fluids the stabilization region is bounded by two critical frequencies. The additional critical frequency arises from the dual role of the fluid's elasticity. This property can act to either stabilize the system by enhancing the overall inertia on account of the memory effect imparted by elasticity or destabilize the system by countering the momentum inertia, depending upon the parametric frequency. Below the lower critical frequency, parametric forcing lowers the threshold for Marangoni instability, destabilizing the system and directly transitioning to a regime where the system is unstable due to both Marangoni and resonant-driven flows with an increase in forcing amplitude. Beyond this critical frequency, parametric forcing stabilizes the system up to an upper critical frequency, similar to Newtonian fluids.

Second, elasticity reduces the forcing amplitude threshold required for stabilization as well as the Faraday instability threshold, with a larger reduction for the Faraday threshold. As a result, even though the threshold for stabilization is lowered, the overall amplitude range where stabilization is achievable becomes smaller due to the inertia-like action provided by the fluid's elasticity.

ACKNOWLEDGMENTS

The authors gratefully acknowledge funding from NSF via grant CBET-2422919 and NASA via grants NNX17AL27G and 80NSSC23K0457. I.B.I. acknowledges support from a Chateaubriand fellowship.

[1] S. J. Vanhook, M. F. Schatz, J. B. Swift, W. D. McCormick, and H. L. Swinney, Long-wavelength surface-tension-driven Bénard convection: experiment and theory, J. Fluid Mech. **345**, 45–78 (1997).
[2] P. Chen, T. Liu, P. Wu, C. Tseng, and C. Leu, Drying-induced birefringence of polyimide optical films, AIChE J. **56**, 790 (2010).
[3] I. B. Ignatius, B. Dinesh, G. F. Dietze, and R. Narayanan, Influence of parametric forcing on Marangoni instability, J. Fluid Mech. **981**, A8 (2024).
[4] U. Thiele, J. M. Vega, and E. Knobloch, Long-wave Marangoni instability with vibration, J. Fluid Mech. **546**, 61 (2006).
[5] S. Shklyaev, A. A. Alabuzhev, and M. Khenner, Marangoni convection in a thin film on a vertically oscillating plate, Phys. Rev. E **92**, 013019 (2015).
[6] K. Kumar and L. S. Tuckerman, Parametric instability of the interface between two fluids, J. Fluid Mech. **279**, 49 (1994).
[7] A. Morozov and S. E. Spagnolie, Introduction to complex fluids, Complex Fluids in Biological Systems: Experiment, Theory, and Computation , 3 (2015).
[8] L. Scriven and C. Sternling, On cellular convection driven by surface-tension gradients: effects of mean surface tension and surface viscosity, Journal of fluid mechanics **19**, 321 (1964).
[9] A. H. Nayfeh, *Perturbation methods* (John Wiley & Sons, 2008).
[10] A. Sobti, A. P. Toor, and R. K. Wanchoo, Oscillatory and steady shear rheological properties of aqueous polyacrylamide solutions, Chem. Data Coll. **17-18**, 356 (2018).
[11] Y. Hirata, Y. Kato, N. Andoh, N. Fujiwara, and R. Ito, Measurements of thermophysical properties of polyacrylamide gel used for electrophoresis, J. Chem. Eng. of Japan **26**, 143 (1993).
[12] W. Guo, G. Labrosse, and R. Narayanan, *The application of the Chebyshev-spectral method in transport phenomena* (Springer Science & Business Media, 2013).
[13] D. Getachew and S. Rosenblat, Thermocapillary instability of a viscoelastic liquid layer, Acta mechanica **55**, 137 (1985).
[14] P. Dauby, P. Parmentier, G. Lebon, and M. Grmela, Coupled buoyancy and thermocapillary convection in a viscoelastic Maxwell fluid, J. Phys.: Condensed Matter **5**, 4343 (1993).
[15] R. Sarma and P. K. Mondal, Marangoni instability in a heated viscoelastic liquid film: Long-wave versus short-wave perturbations, Phys. Rev. E **100**, 013103 (2019).
[16] R. Sarma and P. K. Mondal, Marangoni instability in a viscoelastic binary film with cross-diffusive effect, J. Fluid Mech. **910**, A30 (2021).
[17] H. Müller and W. Zimmermann, Faraday instability in a linear viscoelastic fluid, Europhysics Letters **45**, 169 (1999).
[18] S. Kumar, Parametrically driven surface waves in viscoelastic liquids, Physics of Fluids **11**, 1970 (1999).
[19] A. Lindner and C. Wagner, Viscoelastic surface instabilities, Comptes Rendus Physique **10**, 712 (2009).
[20] F. Schön and M. Bestehorn, Instabilities and pattern formation in viscoelastic fluids, The European Physical Journal Special Topics **232**, 375 (2023).